3D Large scale Marangoni convection in liquid films

M. Bestehorn[1,a], A. Pototsky[1], and U. Thiele[2]

[1] Lehrstuhl für Theoretische Physik II, Brandenburgische Technische Universität Cottbus, Erich-Weinert-Strasse 1, 03046 Cottbus, Germany
[2] Max-Planck-Institut für Physik komplexer Systeme, Nöthnitzer Strasse 38, 01187 Dresden, Germany

Abstract. We study large scale surface deformations of a liquid film unstable due to the Marangoni effect caused by external heating on a smooth and solid substrate. The work is based on the thin film equation which can be derived from the basic hydrodynamic equations. To prevent rupture, a repelling disjoining pressure is included which accounts for the stabilization of a thin precursor film and so prevents the occurrence of completely dry regions. Linear stability analysis, nonlinear stationary solutions, as well as three-dimensional time dependent numerical solutions for horizontal and inclined substrates reveal a rich scenario of possible structures for several realistic fluid parameters.

PACS. 68.15.+e Liquid thin films – 47.20.Dr Surface-tension-driven instability – 68.55.-a Thin film structure and morphology

1 Introduction

Surface structures on (thin) liquid films may arise although surface tension and gravitation stabilize the plane free surface of the film because several other mechanisms are able to destabilize it. The resulting self-organized surface patterns manifest themselves in form of depressed regions or holes. For extremely thin films of thickness in the range under 100 nm the effective molecular interaction between the free surface and the solid support, phenomenologically described by the disjoining pressure, is one of these mechanisms. Another one is present if the fluid is heated from below. Then the surface temperature is proportional to the height and a long wavelength instability may occur if a critical vertical temperature gradient is exceeded. This is due to the Marangoni effect, which denotes the (linear) dependence of surface tension on temperature [1]. A slightly depressed piece of the surface comes closer to the hot bottom plate, heats up and consequently gets a lower surface tension than its surrounding. The resulting surface tension gradient causes a flow away from the depressed piece pulling out even more liquid from this region thereby deepening the depression further. This positive feedback corresponds to an unstable situation.

The evolution in time and space of the instability is normally described by a simplified equation for the profile of the free surface. It can be derived from the Stokes equation using the lubrication approximation [2]. For the thin film on a heated horizontal substrate this was done for a linear dependence of surface tension on temperature by

Burelbach *et al.* [3]. Oron and Rosenau studied the effects of a quadratic dependence of surface tension on temperature [4] and extended the study towards an inclined substrate [5]. In the latter case the evolution equation looses its variational structure allowing for a richer bifurcation structure, as studied recently in some detail by Thiele and Knobloch [6]. All the mentioned work focused on the structure formation in two spatial dimensions, *i.e.* the object of study is a film thickness profile that depends on one spatial coordinate. Pattern formation in three dimensions, *i.e.* the evolution of a film thickness profile that depends on two spatial coordinates was studied by Deissler and Oron for a film on the underside of a cooled horizontal plate where now gravitation acts destabilizing and the surface tension gradient acts stabilizing [7]. Corresponding results for a film on top of a heated plate were given by Oron [8].

Van Hook *et al.* [9] performed extensive experiments on the long-wavelength surface-tension-driven convection for heated horizontal films below a gas layer of finite thickness. They observed both, the formation of depressions (dry spots) and elevations depending on the used gas. They also derived an evolution equation for the film thickness for the used two-layer geometry. It has a similar form as the equation for the one-layer equation but leads to a different definition of the Biot number.

In a different approach Boos and Thess followed numerically the evolution of a film profile towards rupture using the full Stokes equation in combination with a linear temperature field [10]. They found a cascade of consecutive "structuring events" pointing towards the formation of a set of drops as the final state of the system.

[a] e-mail: `bes@physik.tu-cottbus.de`

Due to a slowing down of the numerical scheme once the minimum film thickness becomes very small the final state of the system could not be reached. However, the qualitative agreement between these results and those obtained from long wave approximation [8] indicates that the main features of the physical system are well captured by this approximation, as already noted for falling liquid films [2,11].

In the last few years some theoretical and numerical work was dedicated to pattern formation and instabilities of liquid films in three spatial dimensions [8,12–17]. Especially [8] deals with films unstable due to the Marangoni effect. There, the temporal evolution was restricted due to rupture which occurred when the thickness of the film achieved unphysical negative values. Therefore no results in the long time limit are known up to now. The purpose of the present work is to examine a fluid film in three dimensions under a vertical temperature gradient including a stabilizing effect which is obtained by introducing a disjoining pressure which becomes effective for very small film thickness. Instead of rupture and completely dry domains the solid support is always covered by a thin precursor film of thickness of some 10 nm. This allows to study the long-time evolution of a film unstable due to the Marangoni effect. In the last section we analyze the spatio-temporal evolution of the film surface when a horizontal force is applied externally. This situation is found when the fluid layer is inclined with respect to the vertical. We discuss the formation of periodic structures perpendicular to the slope as well as the instability of fronts moving downwards the inclined plane.

2 The model

2.1 Thin film equation

The commonly used description is based on the hydrodynamic equations with appropriate boundary conditions. We assume a liquid film with mean thickness d, viscosity ν, density ρ, thermal diffusivity κ, and heat conductivity α. On its free upper surface it is in contact with the ambient air having the heat conductivity α_a and thickness d_a. Application of the lubrication approximation [2] allows for the elimination of the velocity field which can be expressed by a single scalar field, namely the height of the film $h(x, y, t)$. At the same order, also the temperature field can be expressed as a function of that state variable. Tangential surface stresses come into play if the surface tension Γ is assumed to be proportional to the surface temperature T_s:

$$\Gamma = \gamma_0 - \gamma(T_s - T_0)$$

where T_0 acts as a reference temperature. The adimensionalized evolution equation describing the height of the film then reads

$$\partial_t h = \nabla \cdot \left\{ \left[h^3 \left(B_o - \frac{\mathrm{d}\Pi}{\mathrm{d}h} - \Delta \right) - \frac{3}{2} h^2 \frac{CM(B+1)}{(1+Bh)^2} \right] \nabla h \right\}$$
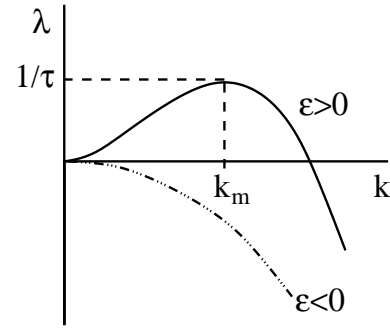
(2.1)

Fig. 1. Sketch of the linear growth rate $\lambda = \varepsilon k^2 - k^4$ in the case of a type-II_s instability. The solid line is above threshold, and dotted-dashed below. Above threshold patterns with the typical length scale $\ell = 2\pi/k_m = 2\pi/\sqrt{\varepsilon/2}$ grow in the linear stage on the time scale $\tau = 4/\varepsilon^2$.

where $\Delta = \partial_{xx} + \partial_{yy}$ is the 2D-Laplacian and

$$M = \frac{\gamma \Delta T d}{\rho \nu \kappa}, \quad B = \frac{\mathrm{d}\alpha_a}{\mathrm{d}_a \alpha}, \quad C = \frac{\rho \nu \kappa}{\gamma_0 d}, \quad B_o = \frac{g \rho d^2}{\gamma_0}$$

denote the Marangoni number, the Biot number, the Crispation number, and the static Bond number respectively. We adopted the scaling of [8], where h and x, y are in units of d and time scales with $3\rho\nu d/\gamma_0$. The temperature ΔT is defined as the difference between the temperature at the bottom and that of the free film surface in the non-convective case. In equation (2.1) the effective molecular interaction between substrate and film surface is taken into account by the disjoining pressure $\Pi(h)$. It will be discussed in detail below in Section 2.2. A linear stability analysis of the flat film without disjoining pressure ($\Pi = 0$) shows that it gets unstable if M exceeds a certain critical value

$$M_c = \frac{2}{3} \frac{B_o}{C}(1 + B) = \frac{2}{3} G(1 + B)$$

(2.2)

where $G = B_o/C$ is the Galileo number.

If M exceeds M_c, a so-called type-II_s [18] instability occurs (Fig. 1) and on the linear (short-time) regime one expects patterns with the typical length scale

$$\ell = 2\pi/\sqrt{\varepsilon B_o}$$

(2.3)

where ε is defined as the reduced distance from threshold

$$\varepsilon = (M - M_c)/M_c.$$

(2.4)

Previous work shows that above the onset of the instability holes are formed and film rupture occurs after a finite evolution time [8]. Thereby rupture is defined by the occurrence of zero film thickness values. Then equation (2.1) is clearly not longer applicable.

However, the possible stationary two-dimensional solutions of equation (2.1) with $\Pi = 0$ can be determined directly [6] independently of the fact that they cannot be reached from the initial condition of a flat film by integration in time. The stationary solutions consist of a vast

Table 1. Values of the adimensional parameters used in the paper.

	water 60 °C		silicone oil 50 cS, 25 °C	
	$\rho = 983$ kg/m^3, $\nu = 4.7 \times 10^{-7}$ m^2/s, $\kappa = 1.6 \times 10^{-7}$ m^2/s		$\rho = 960$ kg/m^3, $\nu = 5 \times 10^{-5}$ m^2/s, $\kappa = 10^{-7}$ m^2/s	
	$\gamma_0 = 6.6 \times 10^{-2}$ N/m, $\gamma = 1.74 \times 10^{-4}$ N/mK		$\gamma_0 = 2.08 \times 10^{-2}$ N/m, $\gamma = 6.8 \times 10^{-5}$ N/mK	
	$d = 10^{-3}$ m	$d = 10^{-6}$ m	$d = 10^{-3}$ m	$d = 10^{-6}$ m
ΔT_c	37 °C	4.3×10^{-5} °C	92 °C	1.07×10^{-4} °C
M_c	86970	1.01×10^{-4}	1308	1.53×10^{-6}
B_o	0.146	1.46×10^{-7}	0.453	4.53×10^{-7}
C	1.12×10^{-6}	1.12×10^{-3}	2.31×10^{-4}	0.23
A	8.0×10^{-15}	8.0×10^{-9}	2.6×10^{-14}	2.6×10^{-8}
A/B_o	5.5×10^{-14}	5.5×10^{-2}	5.6×10^{-14}	5.6×10^{-2}
$\ell \times d$	1.6×10^{-2} m	1.64×10^{-2} m	9.3×10^{-3} m	9.3×10^{-3} m
$h_c^b \times d$	5.5×10^{-8} m	7.1×10^{-7} m	5.5×10^{-8} m	7.3×10^{-7} m

family of drop solutions separated by dry regions of different lengths. All of these solutions are nominally linearly stable since drops separated by dry regions do not interact if no non-hydrodynamic interaction is included. In the formulation without disjoining pressure the solutions with zero microscopic contact angle are energetically favored. However, the inclusion of a disjoining pressure would select a certain contact angle and remove the degeneracy as discussed in [6].

2.2 The disjoining pressure

Now we extend the evolution equation by a disjoining pressure that is of repelling character. It therefore stabilizes a very thin film and avoids the film rupture that restricted the simulations in time to investigations of the short-time behavior. With this extended model we are able to study pattern formation in three dimensions in the long-time limit.

If Van der Waals forces are responsible for the stabilization, the disjoining pressure Π has the form [19,20]

$$\Pi(h) = \frac{A}{h^3} \qquad (2.5)$$

where A is a dimensionless positive constant which is related to the Hamaker constant A_h [21] in the scaling used here by

$$A = \frac{A_h}{6\pi\gamma_0 d^2}. \qquad (2.6)$$

With (2.5), the range of unstable flat films is also bounded from below, *i.e.* flat films with the height $h = h_0$ are unstable if

$$h_c^b \le h_0 \le h_c^t. \qquad (2.7)$$

The two values h_c^b and h_c^t are named *spinodals*. For thick films in the millimeter range, one finds the scaling $h_c^b \propto d^{-1/3}$. The values of h_c^b are very small in the range of

$10^{-7}...10^{-8}$ m (see Tab. 1). Approximately flat parts of the film profile which have a thickness in the stable region below h_c^b can be considered as a precursor film. They cover the substrate even in regions where the dry spots occur with the height in the range of some 10 to 100 nm.

We note that the inclusion of the disjoining pressure changes the value for M_c to

$$M_c = \frac{2}{3}\frac{B_o}{C} + 2\frac{A}{C}. \qquad (2.8)$$

Here we approximated $(1 + B)$ by 1, which is good for small Biot number, *i.e.* for a thermally almost insulating upper boundary. We shall use this approximation for the rest of the paper.

2.3 Fluid parameters

To compare with the experiments we show in Table 1 the values of the adimensional parameters introduced above as well as those of some important properties of the fluid film. To demonstrate also the dependence on the film thickness, we choose the four cases water and silicone oil, each with layer thicknesses of 1 mm and 1 μ. For the Hamaker constant we took the value $A_h = 10^{-20}J$ from [22]. The typical length scale ℓd is computed from (2.3) for $\varepsilon = 1$. It is remarkable that for thin films the critical Marangoni number as well as the applied temperature gradients seem to be very small. This means in real experiments one would usually exceed the critical point by a factor of some thousands. However, in a film of 1 mm depth, the value of M_c in silicone oil is already much larger than that for small scale convection (about 80...100). Consequently to obtain a pure surface instability without small convective cells (hexagons) the liquid depth should be below 1 mm. We note that in the case of a fluid depth where both instabilities may occur, pattern formation is expected to be much more involved and the small scale structure cannot longer be eliminated using the lubrication approximation.

In this case the full system including Navier-Stokes as well as heat equation has to be considered. A detailed linear analysis was done by Golovin *et al.* [23].

3 Stationary solutions

3.1 Holes, drops, and walls

In the case of stationary solutions equation (2.1) can be integrated twice which yields

$$\frac{1}{B_o}\Delta h = -\frac{\mathrm{d}}{\mathrm{d}h}V(h) - \mu \qquad (3.1)$$

with

$$V(h) = -\frac{1}{2}h^2 - \frac{\alpha}{6}\frac{1}{h^2} + (1+\varepsilon)(1+\alpha)h(\ln h - 1) \quad (3.2)$$

beyond the small bifurcation parameter ε defined in (2.4) we have introduced the reduced Hamaker constant α

$$\alpha = \frac{3A}{B_o}$$

which enters the equation as the only parameter that depends on the material. As already shown in [7], the integration constant μ is fixed by the mean value of $\mathrm{d}V/\mathrm{d}h$ which follows from (3.1) by integration over the spatial domain A (periodic lateral b.c.):

$$\mu = -\frac{1}{A}\int_A \mathrm{d}x\mathrm{d}y\frac{\mathrm{d}}{\mathrm{d}h}V(h).$$

In the 2D-case Thiele *et al.* studied extensively a similar problem in the case of dewetting. There the disjoining pressure contributes both, the destabilizing long-range and the stabilizing short-range, components [24–26], whereas here they are given by the Marangoni effect and the stabilizing disjoining pressure, respectively. For the functions $V(h)$ they used it was found, that the system has three qualitatively different solutions: drop-, hole- and wall-solutions. The 3D-case is, however, qualitatively different from the two-dimensional one. First, it is not so simple any more to solve (3.1) by reducing it to an ordinary differential equation. Second, even if we have found some special numerical solutions, we still cannot say anything about other solutions, since the function space in 3D is much more complicated than in 2D.

In this section we wish to focus on radial symmetric solutions reducing again the spatial dimension by one and state conditions where the types known from the 2D computations may occur. To obtain an effective one-dimensional equation we use polar coordinates in (3.1). For such a radial-symmetrical function $h(r)$ we have the following equation (see also the discussion in [7]):

$$\frac{\mathrm{d}^2h}{\mathrm{d}r^2} + \frac{1}{r}\frac{\mathrm{d}h}{\mathrm{d}r} = -\frac{\mathrm{d}}{\mathrm{d}h}V(h) - \mu. \qquad (3.3)$$

In the 2D-case it was possible to rewrite (3.1) in the "energy-conservation" form [6,26]:

$$\frac{1}{2}\left(\frac{\mathrm{d}h}{\mathrm{d}x}\right)^2 + V(h) + \mu(h - h_0) = E. \qquad (3.4)$$
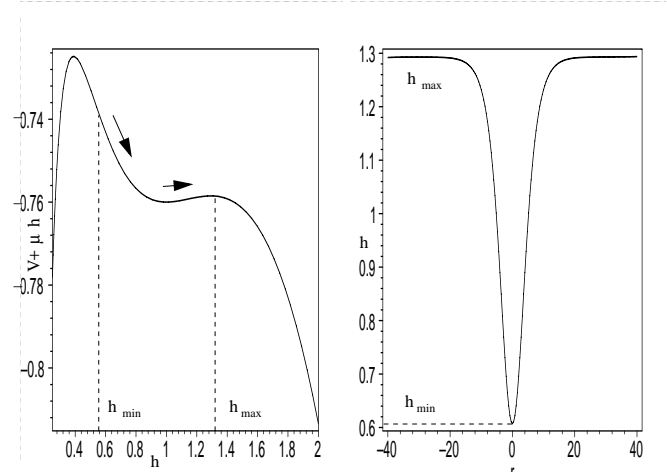

Fig. 2. Left: Hole solution in the case of radial symmetry. The effective energy $V(h) + \mu h$ is shown on the left image. The hole solution corresponds to the classical motion of a particle in the potential: trajectory starts at point $r = 0$ with the height $h(r = 0) = h_{min}$, this is between the left maximum and the minimum of the effective energy. The height of the film increases monotonically to the value corresponding to the right maximum of the effective energy. The period of such a solution is infinitely large.

Using the formal equivalence of this equation to the equation of motion for a particle in a potential V, when seeing x as "time" one could find all main features of stationary solutions by studying the effective potential energy $V(h) + \mu h$. Equation (3.3), however, contains an additional term that explicitly depends on r. This leads to the fact, that the "energy" is no longer conserved along the "trajectory". Equation (3.3) may describe some mechanical system with "time"-dependent friction $\frac{1}{r}\frac{\mathrm{d}h}{\mathrm{d}r}$. It is still possible to analyze the behavior of such a "mechanical" system by studying its effective energy. The function $V(h) + \mu h$ with V given as (3.2) is shown on the left images of Figures 2 and 3 for different values of μ. In all cases this function has two maxima and one minimum, but in Figure 2 the left maximum is higher then the right one, in Figure 3 the left one is lower then the right one. Further we are looking for the solutions of (3.3) with the "initial condition": $(\frac{\mathrm{d}h}{\mathrm{d}r})_{r=0} = 0$. Each value of $h(r)$ corresponds to a point on the effective energy curve. The real film profile is given by the motion of such a point along the curve $V(h) + \mu h$. If equation (3.3) describes a mechanical system with "time"- dependent friction, we can say the following about possible stationary states:

In the wide range of initial heights, (the film thickness at the origin) $h(r = 0)$, between the maxima of the effective energy (Fig. 4), there exist damped periodical or even unbounded solutions, that have no direct physical meaning. However, if rotational symmetry is broken the damped oscillations in r may be associated with satellite holes observed for dewetting in simulations by Kargupta *et al.* [27]. But among such solutions, there exist three solutions with infinitely large period. These are similar to the drop-, hole- and wall-solutions from [25,26,28].
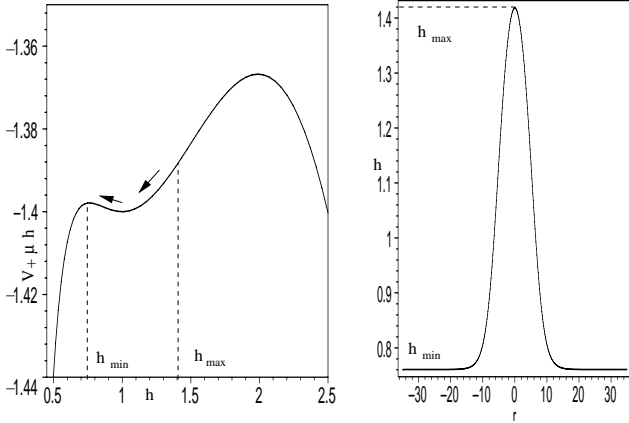
Fig. 3. Drop solution. As in Figure 2, the curve starts at $r = 0$ between the right maximum and the minimum of the effective energy. The height of the film decreases monotonically to the left maximum.
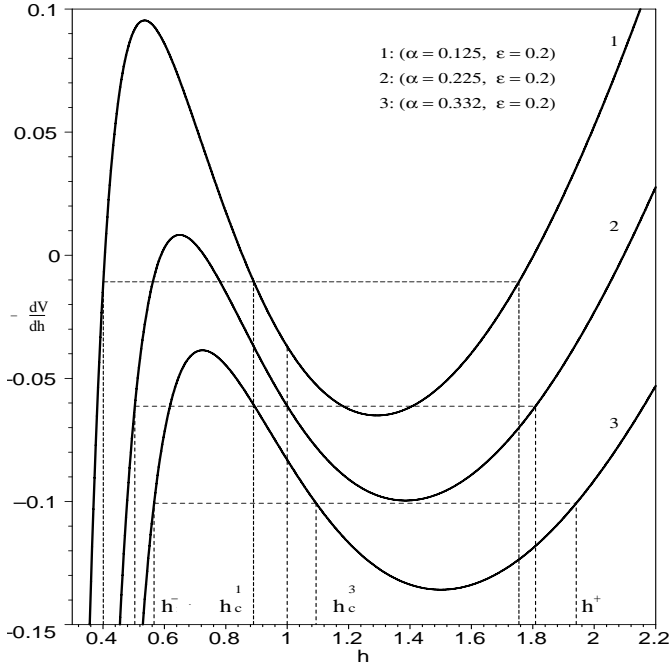

Fig. 4. The disjoining pressure $d_h V(h)$ according to (3.2) for different values of α and $\varepsilon = 0.2$. The critical film depth h_c is obtained by a Maxwell-equal-area construction for each potential. If $h_c < 1$ (thick film) holes are energetically preferred, otherwise drops will be formed in the nonlinear stage. Between the two extrema (the spinodals) the film is absolutely unstable, between h^- and h^+ (the binodals) it is bistable.

1) Hole-solution: the initial height is somewhere between the left maximum and the minimum of the effective energy (see Fig. 2), the "mechanical" system starts to move to the right along the curve of effective energy, passes the minimum with the highest "velocity" $\frac{dh}{dr}$, and continues to the right maximum $h = h_{max}$. This process takes an infinitely long "time" $r \to \infty$. In order to proof that we linearize $d_h V(h)$ at $h = h_{max}$. Since $-d_h V(h =$

$h_{max}) - \mu = 0$ and since $-d_{hh}V(h = h_{max}) > 0$, we have instead of (3.3):

$$\frac{d^2 h}{dr^2} + \frac{1}{r}\frac{dh}{dr} - \omega^2(h - h_{max}) = 0 \qquad (3.5)$$

here is $\omega^2 = -d_{hh}V(h = h_{max})$.

The solution of the last equation is the first Bessel function $(m = 0)$: $h(r) = h_{max} - K_0(\omega r)$. Since K_0 has the property: $\lim_{r \to \infty} K_0(r) = 0$, it is clear that only for $r = \infty$ the hole-solution reaches h_{max}.

2) Drop-solution: the initial height is somewhere between the right maximum and the minimum (Fig. 3). This case is similar to the hole-solution. The only difference is that $h(r)$ decreases monotonic to h_{min}. The proof that the drop-solution has infinitely large period is similar to the case of the hole-solution.

3) Wall-solution: the values of two maxima of the effective energy are equal. The initial height of the film is $h = h_{in}$. Let the motion start at the left maximum. But now it takes infinitely long to leave the initial point and the "damping" plays no role for this type of motion. For $r = \infty$ the height h passes through the minimum of the effective energy, and continues to the right maximum. The film profile in this case is similar to the hole-profile, with the difference that the size of the hole is now infinitely large. This corresponds to a zero curvature of the whole, *i.e.* a plane front.

3.2 Holes or drops?

For the experiment as well as for the numerical solutions of the next paragraph it is important to know whether drops or holes are formed in the unstable range of the flat film $\varepsilon > 0$. Assuming that the flat film has the height $h_0 = 1$ this can depend only on the values of ε and α. Figure 4 shows plots of the pressure $d_h V(h)$ for several values of these parameters. If $h_0 = 1$ lies on the left-hand-side of the critical film depth $h = h_c$ (Maxwell point), drops are energetically preferred, in the other case holes are expected. The condition that $h_0 = 1$ coincides with the Maxwell point allows to compute α as a function of ε, as done in Figure 5. From that figure it is clear that for small values of the reduced Hamaker constant holes should be observed. But it is interesting that for $\alpha > 1/3$ drops are the only possible structures. Since $\alpha \propto d^{-4}$ this means that for very thin films always drops evolve, whereas for thicker ones the pattern at onset consists of holes but turns to drops for larger temperature gradients far from threshold. From these calculations one would expect drops even in rather thick films, but farther from threshold as a kind of secondary instability.

However, the depth of the precursor film may decrease slightly if the physical thickness of the flat film is very large (Fig. 6). For thin precursor films the validity of equation (2.1) seems not longer justified and one cannot say from the present theory if rupture occurs or not. But even for a thick film with $d = 1$ mm (at $\varepsilon = 5$) we compute the height of the precursor film to 10 nm. As already mentioned in Section 2.3, for fluids above a certain thickness, small scale
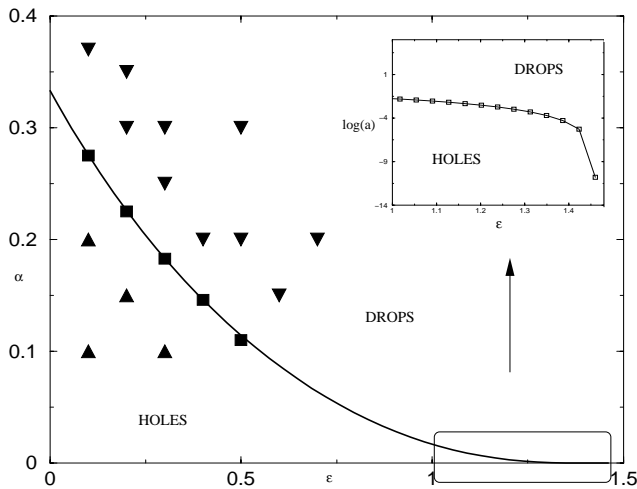
Fig. 5. Phase diagram in the parameter plane. The codimension-one line results from the condition $h_c = h_0$ (cf. Fig. 4 and text). Solving the fully time dependent equation (4.1) numerically, one obtains mazes (squares), holes (up-triangles) and drops (down-triangles) in excellent agreement with the theory. The inset shows that there is a finite $\varepsilon \approx 1.47$ above which drops mathematically exist even at $\alpha = 0$.
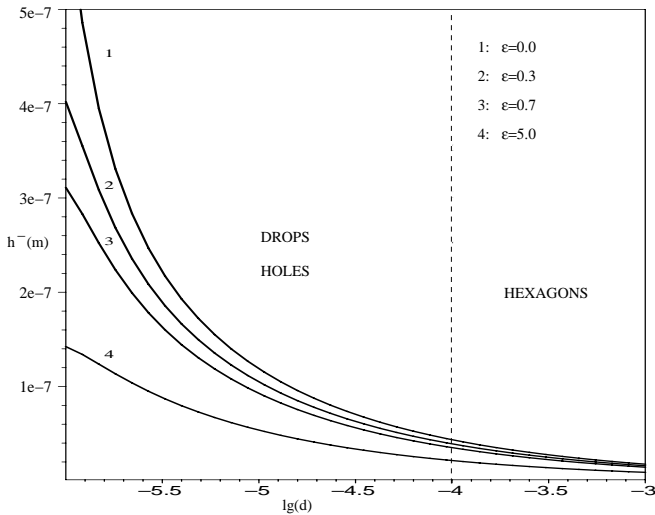

Fig. 6. The thickness h^- of the precursor film as a function of the mean film thickness d, both in physical units (m). For increasing d the precursor film becomes thinner and would finally vanish. But right from the dashed line, small scale convection sets in (silicone oil) in form of hexagons and the description used here is not valid in this part. In water, small scale convection would set in for even smaller values of $d \approx 0.1$ mm.

motion sets in first leading to the well known hexagonal convection cells.

4 Fully time dependent 3D-solutions

4.1 Normal form

To obtain numerical results in three dimensions, we first transform equation (2.1) into a more convenient form. Introducing the reduced control parameter ε according to

(2.4) and after rescaling of space and time variables, it takes the form

$$\partial_t u = -\varepsilon \Delta u - \Delta^2 u + \nabla \cdot [f(u, \Delta) \nabla u]. \quad (4.1)$$

Here,

$$u(x, y, t) = h(x, y, t) - 1$$

is the normalized, shifted height with vanishing mean value. Space and time are scaled again to (the primes are omitted in (4.1))

$$x = x'(B_o + 3A)^{-1/2}, \qquad t = t'(B_o + 3A)^{-2}$$

in (4.1), $f(u, \Delta)$ stands for the operator function

$$f(u, \Delta) = \frac{1}{1+\alpha} \left[(1+u)^3 - 1 - \frac{\alpha u}{1+u} \right] \\ - (1+\varepsilon) \left[(1+u)^2 - 1 \right] - \left[(1+u)^3 - 1 \right] \Delta \quad (4.2)$$

which vanishes with u. Note that this form contains only one material parameter, namely α. Equation (4.1) can be considered as a kind of normal form for pattern formation of this type, at least its linear part. The dispersion relation shown in Figure 1 is obvious, the linearly fastest growing mode has the wave vector $k_m = \sqrt{\varepsilon/2}$ and grows with the typical rate $\tau = 4/\varepsilon^2$. The nonlinear part (as well as the linear one) has the form of the divergence of a flux and clearly conserves the mean value of u to zero. We note in passing that the lowest order truncation $O(\varepsilon^3)$ of (4.1) reads

$$\partial_t u = -\varepsilon \Delta u - \Delta^2 u + \nabla(u \nabla u) \quad (4.3)$$

and coincides with the lowest order truncation of the Knobloch equation [29].

4.2 The numerical method

To solve equation (4.1) numerically, it is of advantage to use a semi-implicit time integration scheme [30,31]. The linear parts of (4.1) are therefore taken at the new time step $t + \delta t$, the nonlinearities at t. This allows for a much larger time step than a fully explicit method. Approximation of the time derivative by the first order differential quotient leads to the relation

$$\left[\frac{1}{\delta t} + \varepsilon \Delta + \Delta^2 \right] u(t + \delta t) = \frac{1}{\delta t} u(t) + \nabla(f \nabla u(t)). \quad (4.4)$$

To solve for $u(t + \delta t)$ one has to invert the linear differential operator in square brackets on the left hand side of (4.4). Assuming periodic lateral boundary conditions in real space, this can be done best in Fourier space:

$$\tilde{u}_k(t + \delta t) = \left[\frac{1}{\delta t} - \varepsilon k^2 + k^4 \right]^{-1} \tilde{\Phi}_k(t) \quad (4.5)$$

where $\tilde{u}_k$ denotes the Fourier transform of u and $\tilde{\Phi}_k$ that of

$$\Phi(t) = \frac{1}{\delta t} u(t) + \nabla(f \nabla u(t)). \quad (4.6)$$

To avoid singularities, the expression in the square bracket in (4.5) must be positive for all k, yielding an upper bound of the time step

$$\delta t_{max} = 4/\varepsilon^2$$

which is rather large since ε is usually of order 0.1. We note that numerical stability is already lost for much smaller time steps then δt_{max} due to the explicit terms on the right hand side of (4.4). In all runs described below we fix the time step in the region $0.1 < \delta t < 1$.

The numerical scheme must fulfill the conservation of the mean height, *i.e.*

$$\int \mathrm{d}x \mathrm{d}y\, u(t) = 0$$

must hold for all times. In Fourier space this is equivalent to

$$\tilde{u}_0(t) = 0$$

which is fulfilled for all time steps if $\tilde{\Phi}_0 = 0$. From (4.6) it follows that

$$\int \mathrm{d}x \mathrm{d}y\, \nabla(f\nabla u(t)) = 0 \qquad (4.7)$$

must vanish, which is obvious for periodic boundary conditions. Numerically, the validity of (4.7) may depend on the way how the derivatives in real space of u are computed. We use a centered space finite difference method which clearly satisfies (4.7). This ensures conservation of $\int \mathrm{d}x \mathrm{d}y\, u(t)$ up to the numerical precision which is of order 10^{-8}.

4.3 The horizontal layer

To show the temporal evolution of the film we present runs for several parameter values in the $\varepsilon-\alpha$ plane. For all runs that follow random dot initial conditions have been used with vanishing mean value. We take a large aspect ratio of 520, in units of equation (4.1), what corresponds to about 0.5 m for the silicon oil of Table 1. This of course is a very large value, expressing the huge scale of the structure, which is due to the small supercriticality of $\varepsilon = 0.1$. Starting with the relatively large value of $\alpha = 0.35$ (rather thin film) drops are expected even at onset. This can be seen in the evolution of Figure 7 where larger and larger drops are found with increasing time. We note that the evolution times are extremely long, also a consequence of the small supercriticality (see also the remarks in Sect. 2.3).

Next we use the smaller value $\alpha = 0.05$, corresponding to a thicker film. Holes are formed now quite early (Fig. 8). As can be also seen a small depression is formed along the border of each hole. The long-time behavior can be compared with that of drops. One observes a coarsening of the holes as for the drops. Eventually all holes (drops) merge into a single big hole (drop). However, this process may take a very long time, depending on the several fluid parameters and the geometry of the layer.

To examine the temporal behavior further, we compute the mean modulus of the wave vector in Fourier space
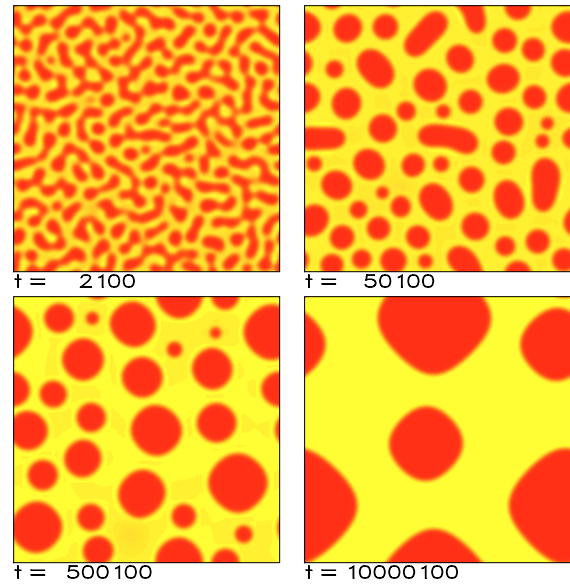

Fig. 7. Time series found by numerical integration of (4.1) in the drop regime at $\varepsilon = 0.1$ and $\alpha = 0.35$. The numerical resolution is 256×256 mesh points, the aspect ratio (length to depth) 520. Dark regions correspond to an elevated surface. Periodic boundary conditions are assumed in the lateral directions.
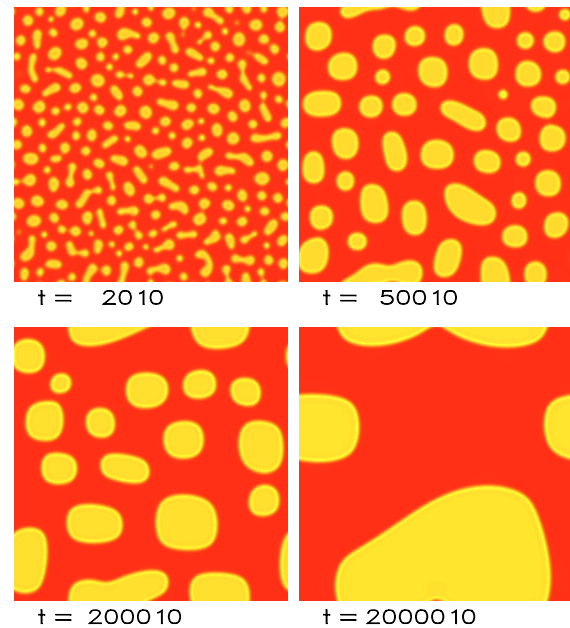

Fig. 8. Time series in the hole regime at $\varepsilon = 0.1$ and $\alpha = 0.05$.

according to

$$\langle k \rangle = \frac{\int \mathrm{d}^2 k\, |u_k|^2 |\mathbf{k}|}{\int \mathrm{d}^2 k\, |u_k|^2}.$$

From Figure 9 a scaling law of the form

$$\langle k \rangle = ct^{-\beta} \qquad (4.8)$$

can be clearly extracted. It is remarkable that the exponent for both series, *i.e.* drops and holes, is almost the same. We found it to be $\beta \approx 0.21$.

Finally, we present a parameter pair directly on the critical line of Figure 5. As expected, the decision between
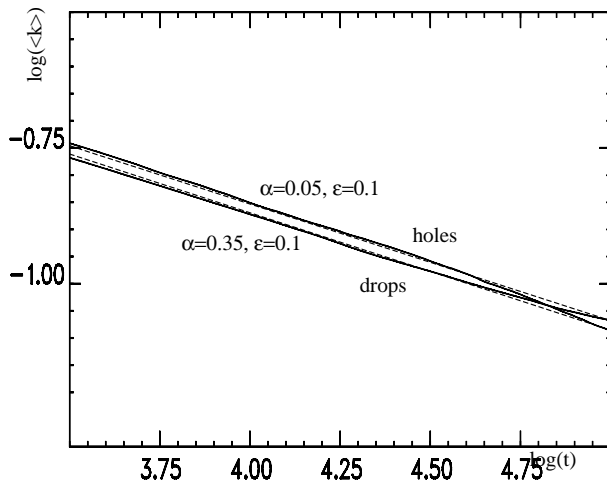
Fig. 9. The solid lines show the typical scaling of the mean modulus of the wave vector in the temporal evolution for parameters as in Figures 7 and 8. The scaling exponent for both series is the same, $\beta \approx 0.21$ as indicated by the dashed lines. For this computation, we used twice the system size of Figures 7 and 8, and a numerical resolution of 512×512 points.
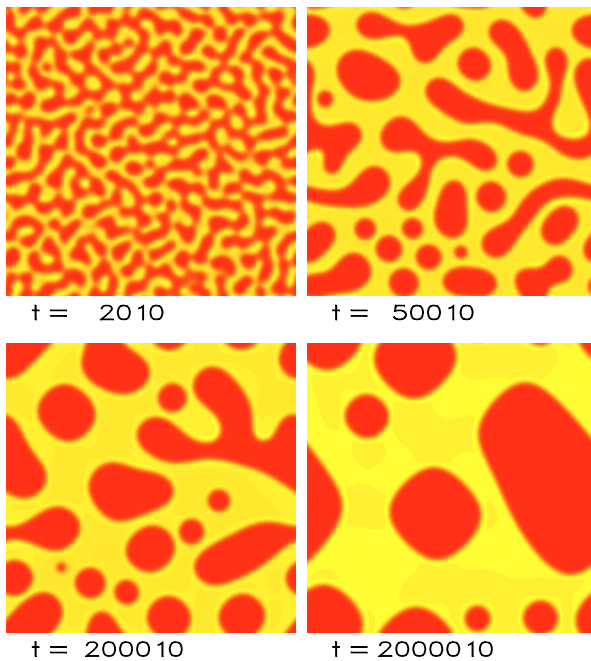

Fig. 11. Dynamical scaling of the maze pattern for parameters as in Figure 10. The scaling exponent is again $\beta \approx 0.21$ (dashed line).

Fig. 10. Time series in the maze regime at the codimension-one line of Figure 5 ($\varepsilon = 0.1$, $\alpha = 0.28$).

Fig. 12. Small drops inside big holes are formed if the heating is suddenly increased and ε crosses the phase line of Figure 5. The series was started with $\varepsilon = 0.01$ and $\alpha = 0.3$, After $t = 443,370$ we increased ε to $\varepsilon = 0.15$.

drops and holes is not clear and a kind of maze structure remains for long times (Fig. 10). But also these mazes show the typical dynamics to longer and longer horizontal scales with the same exponent $\beta \approx 0.21$ as shown in Figure 11.

In Section 3.2 we discussed the possibility of a secondary instability of holes with respect to drops if ε is increased and the codimension-one line of Figure 5 is crossed. To examine this situation further we comput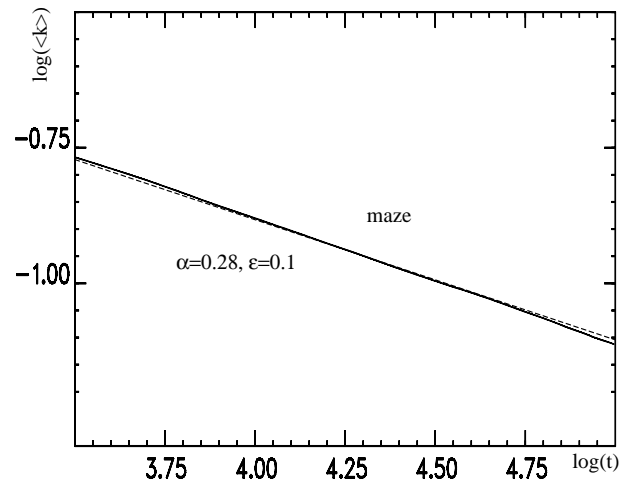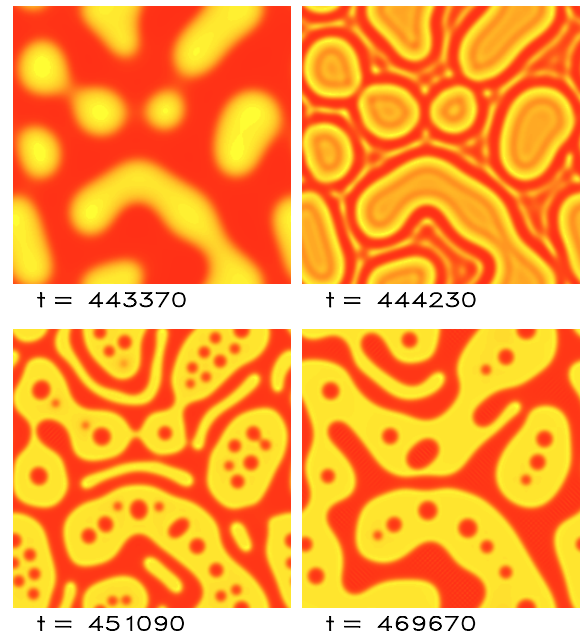e a temporal evolution of a randomly distributed initial pattern with $\varepsilon = 0.01$ and $\alpha = 0.3$ in the hole region. Figure 12, first frame, shows the formation of holes. After switching ε to a larger value in the drop region small drops are formed rather quickly inside the holes. In this way, drops with a super-structure left from the holes emerge.

4.4 The inclined layer

In this section, we study the influence of a constant external force in a certain horizontal direction. This can be due either to an inclination of the layer by an angle φ, or to an additional horizontal temperature gradient. Here, we
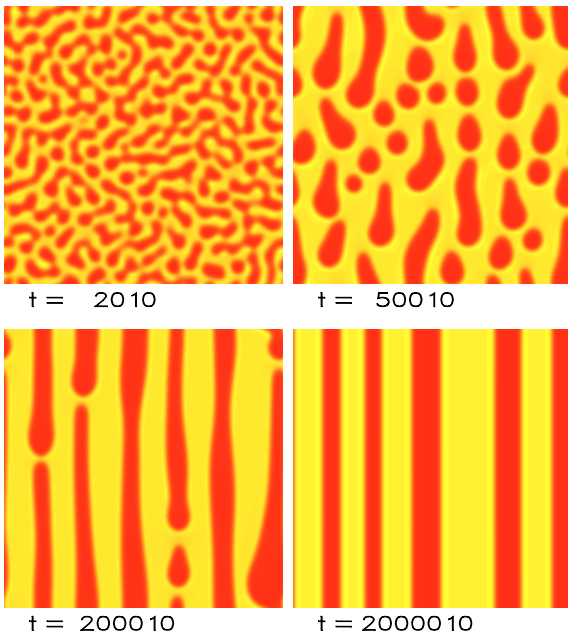
Fig. 13. Pattern formation in the inclined film. Parameters are those of Figure 7 but the fluid is very slightly inclined in vertical direction. After the linear stage, the pattern gets anisotropic and finally a periodic structure of parallel fluid pipes with a certain wavelength is stabilized.

shall concentrate on the first case. A constant body force gives an additional term of the form (small $\varphi \approx \sin\varphi$) [5]

$$B_o \varphi \mathbf{n} \cdot \nabla \left(h^3 \right)$$

on the right hand side of (2.1). Here, $\mathbf{n}$ is the direction of inclination. For the simulation periodic boundary conditions are kept in all directions.

The inclination even by a very small angle φ completely changes the pattern morphology in the long time limit. This is shown in Figure 13 where all parameters are equal to that of Figure 7 but the plane was inclined by an angle of order $0.1°$ (for a silicone film of thickness 1 mm). At the beginning both evolutions seem to be similar but after $t \approx 30,000$ in the inclined film coarsening is retarded orthogonally to the inclination and finally a certain wavelength is stabilized. The stripes orientate more and more along the direction of inclination, forming a structure of more or less equally spaced pipes or rivulets where the fluid flows down inside. The effect of inclination on the dynamical scaling law (4.8) can be seen from Figure 14.

Finally we study the influence of a constant force perpendicular to a channel of depressed liquid. To this end we start the numerical integration with the initial condition

$$u(x,y,t=0) = \begin{cases} -0.77 & \text{for } 0 \leq y \leq L/8 \\ 0.11 & \text{for } L/8 < y < L \end{cases}$$

where L is the total length of the layer. Both heights, the elevated as well as the depressed lay outside the spinodal region, *i.e.* the flat film in these parts is stable. To avoid the unphysical homogeneity in x-direction of the
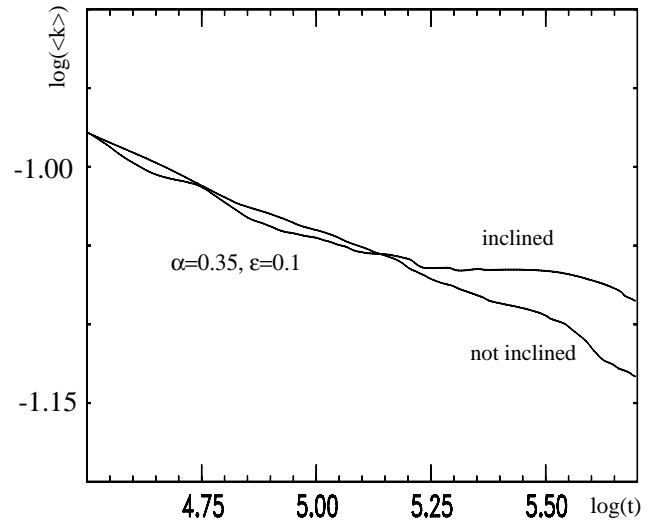

Fig. 14. Comparison of the dynamical scaling of inclined and plane case. After $t \approx 100,000$ the stabilization of the wavelength in the inclined case can be clearly seen.
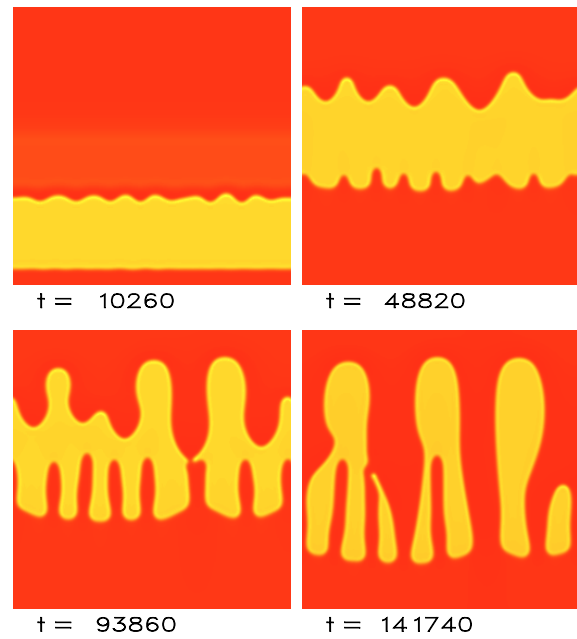

Fig. 15. Evolution of a channel on an inclined plane. Parameters are those of Figure 8 in the hole regime. Both edges of the channel get unstable on different time scales. The trailing edge is disturbed faster with a larger wavelength. Finally the two edges meet on several points and the channel separates.

initial condition we add small fluctuations of about 1 per cent. The layer in this numerical experiment is inclined by about $1°$ (if the fluid is a silicone oil film with depth 1 mm). Then the channel moves with the average velocity of $\approx 1\,\text{mm/sec}$. After about $t = 10,000$ (corresponding to about 300 sec) a phase instability of the back front of the channel (or the leading front of the elevated part) can be clearly observed (Fig. 15). Later on, the opposite front gets unstable with a smaller wavelength as studied for a liquid ridge on an inclined plate in [32]. At this stage,

both fronts are well separated and can be considered as being independent from each other. This changes if the front instabilities evolve further. The channel gets more and more restricted by the respective advancing and receding fingers and finally breaks in several isolated holes. The final situation after a rather long evolution resembles that of Figure 13.

5 Conclusion

In the present paper we studied a thin liquid layer with a free surface heated from below. We considered the case where the fluid is unstable due to the Marangoni effect against large scale surface deformation but small scale convection cannot occur. To describe pattern formation under these circumstances, we used the lubrication approximation and concentrated on the properties and solutions of the thin film equation, derived from the basic set of hydrodynamic equations. In addition to previous work [5,6,8] our description includes a repelling van der Waals term as disjoining pressure which accounts for stabilization of extremely thin fluid layers of 10 to 100 nm height. Rupture obtained earlier as a singularity of the thin film equations without disjoining pressure is now avoided in this way and the spatio-temporal evolution of surface patterns can be studied in the long time domain. Instead of forming completely dry regions, the substrate remains now always covered with such a thin fluid layer or precursor film.

The linearized problem and the energy method allows for computation of the stability regions of (circular) drops, holes, or fronts with respect to the vertically applied temperature gradient and the mean film thickness. We showed that on very thin films drops should always evolve at onset. For thicker films, we predict the formation of holes at onset which then, for higher values of the Marangoni numbers, should give way to drops. We note that drops, or at least one big drop on a rather thick film was found in the experiment by Van Hook *et al.* for an air layer, instead of holes for an helium gas layer above a silicone film [9]. The thermal properties of the gas layer influence the Biot number and also the Marangoni number. It seems possible that the Helium experiment was performed closer to threshold than the one with the air layer. According to our stability analysis this would explain the patterns observed in this experiment.

In the last section we studied the film behavior in three spatial dimensions, solving the two-dimensional film equation numerically. We found holes, drops and mazes for several parameter settings. An exponential scaling law of the wavelength could be extracted from the numerical runs. We found an independent scaling factor with respect to the Hamaker constant close to threshold. The scaling law $k \sim t^{-\beta}$ with $\beta = 0.21 \pm 0.01$ indicates that the coarsening is slower than in spinodal decomposition, where $\beta = 1/3$ as given by the Lifshitz-Slyozov-Wagner theory (see for example [33]). The inclusion of hydrodynamic effects in the description of spinodal decomposition give even larger

exponents for the long time limit (in 2D: $\beta = 1/2$ viscosity controlled, $\beta = 2/3$ inertia controlled [34]).

However, the exponent found here is similar to $\beta = 0.22$ found in numerical simulations for spinodal decomposition with a mobility that depends strongly on concentration implying the prevalence of surface diffusion over bulk diffusion [35]. A scaling argument for this case yields $\beta = 1/4$ [35]. To our knowledge for spinodal dewetting there exist no analytic or numeric results for the scaling exponent in two dimensions (for one dimension see [36]).

Finally we turned to the case of a slightly inclined layer under gravitation. Here we demonstrated the influence of inclination on the dynamical scaling as well as on the formation of front instabilities and fingers. The found transversal instabilities of leading and trailing edges of elevated regions or liquid ridges show behavior reminiscent of the front and back instabilities of liquid ridges on an inclined plane studied in [32,37]. Especially, it should be noted that the instabilities at trailing and leading edge are seemingly independent corresponding to the decoupled regime in [32]. The wavenumber at the back is also nearly twice as large as the one at the front. The studied system could be especially suited to investigate the fingering at the back experimentally, because following the analogy with the results of [32] the destabilizing influence for the transversal instability is given by the heating. The heating can be exactly controlled and changed experimentally and so its influence on the characteristics of the instability can be investigated directly. On the contrary the destabilizing influence in [32] is the long-range part of the disjoining pressure that is difficult to control.

Finally we mention that to our knowledge there exists no theory for the mechanism of nonlinear wavelength selection and stabilization of a periodic structure in the inclined case, which can be clearly seen from our numerical simulations.

References

1. A.A. Nepomnyashchy, M.G. Velarde, P. Colinet, *Interfacial phenomena and convection* (Chapman & Hall/CRC, Boca Raton, 2002)
2. A. Oron, S.H. Davis, S.G. Bankoff, Rev. Mod. Phys. **69**, 931 (1997)
3. J. Burelbach, S. Bankoff, S. Davis, J. Fluid Mech. **195**, 463 (1988)
4. A. Oron, P. Rosenau, J. Fluid Mech. **273**, 361 (1994)
5. A. Oron, P. Rosenau, J. Phys. II France **2**, 131 (1992)
6. U. Thiele, E. Knobloch, submitted to Physica D (2003)
7. R.J. Deissler, A. Oron, Phys. Rev. Lett. **68**, 2948 (1992)
8. A. Oron, Phys. Fluids **12**, 1633 (2000)
9. S.J. VanHook, M.F. Schatz, J.B. Swift, W.D. McCormick, H.L. Swinney, J. Fluid Mech. **345**, 45 (1997)
10. W. Boos, A. Thess, Phys. Fluids **11**, 1484 (1999)
11. B. Ramaswamy, S. Chippada, S.W. Joo, J. Fluid Mech. **325**, 163 (1996)
12. A. Oron, Phys. Rev. Lett. **85**, 2108 (2000)
13. A. Sharma, R. Khanna, Phys. Rev. Lett. **81**, 3463 (1998)
14. A. Sharma, R. Khanna, J. Chem. Phys. **110**, 4929 (1999)

15. L. Schwartz, R.V.Roy, R.R. Eley, S. Petrash, J. Colloid Interface Sci. **214**, 363 (2001)
16. J.A. Diez, L. Kondic, Phys. Rev. Lett. **86**, 632 (2001)
17. M. Bestehorn, K. Neuffer, Phys. Rev. Lett. **87**, 046101 (2001)
18. M.C. Cross, P.C. Hohenberg, Rev. Mod. Phys. **65**, 851 (1993)
19. R.J. Hunter, *Foundation of Colloid Science*, Vol. 1 (Clarendon Press, Oxford, 1992)
20. J.N. Israelachvili, *Intermolecular and Surface Forces* (Academic Press, London, 1992)
21. C.J. Van Oss, M.K. Chaudhury, R.J. Good, Chem. Rev. **88**, 927 (1988)
22. M.J. Tan, S.G. Bankoff, S.H. Davis, Phys. Fluids A **2**, 313 (1990)
23. A.A. Golovin, A.A. Nepomnyashchy, L.M. Pismen, Phys. Fluids **6**, 34 (1994)
24. U. Thiele, M.G. Velarde, K. Neuffer, Phys. Rev. Lett. **87**, 016104 (2001)
25. U. Thiele, M.G. Velarde, K. Neuffer, Y. Pomeau, Phys. Rev. E **64**, 031602 (2001)
26. U. Thiele, K. Neuffer, Y. Pomeau, M.G. Velarde, Colloid Surf. A **206**, 135 (2002)
27. K. Kargupta, R. Konnur, A. Sharma, Langmuir **17**, 1294 (2001)
28. V.S. Mitlin, J. Colloid Interface Sci. **156**, 491 (1993)
29. E. Knobloch, Physica D **41**, 450 (1990)
30. C.A.J. Fletcher, *Computational Techniques for Fluid Dynamics*, Vol I (Springer Press, Berlin, 1989)
31. M. Bestehorn, Phys. Rev. E **48**, 3622 (1993)
32. U. Thiele, E. Knobloch, Phys. Fluids **15**, 892 (2003)
33. J.S. Langer, *An introduction to the kinetics of first-order phase transitions*, edited by C. Godreche (Cambridge University Press, 1992), Chap. 3, pp. 297–363
34. I. Podariu, Z.Y. Shou, A. Chakrabarti, Phys. Rev. E **62**, R3059 (2000)
35. A.M. Lacasta, A. Hernández-Machado, J.M. Sancho, R. Toral, Phys. Rev. B **45**, 5276 (1992)
36. K.B. Glasner, T.P. Witelski, Phys. Rev. E **67**, 016302 (2003)
37. U. Thiele, K. Neuffer, M. Bestehorn, Y. Pomeau, M.G. Velarde, Colloid Surf. A **206**, 87 (2002)